Available online at www.sciencedirect.com

ScienceDirect

Procedia Manufacturing 30 (2019) 231–238

Procedia MANUFACTURING

www.elsevier.com/locate/procedia

14th Global Congress on Manufacturing and Management (GCMM-2018)

Effects of surface topography and chemistry modifications of stainless steel through ion implantation on icephobicity

Thomas Loho[a*], Jerome Leveneur[b], John Kennedy[b]

[a]*University of Auckland,4-6 Park Avenue, Grafton, Auckland 1023, New Zealand*
[b]*National Isotope Centre, GNS Science, Lower Hutt 5010, New Zealand*

Abstract

The adhesion of ice onto various surfaces can lead to many problems in the engineering world, creating hazards and economic losses. Recently, passive icephobic surfaces have been developed that can prevent ice build-up on a surface, but the mechanism of ice adhesion to a surface is still not well understood. This study aims to improve the understanding of the mechanism of ice adhesion to stainless steel surfaces. Ion implantation with Xe^+ ions was used for surface topography modifications and CF^+ ions were used for surface chemistry modifications. The effect of a combination of both treatments was also investigated. The results of this study confirm the theory that the ice adhesion strength of a material is determined by the degree of interaction between ice and the material at the ice-solid interface. An ice droplet that penetrates into the space between asperities (Wenzel-type) shows higher ice adhesion strength than an ice droplet that sits on top of the asperities and microscopic air bubbles (Cassie-Baxter type). It was suggested that because hydrophobic substances were implanted near the base of the asperities, the transition of a Cassie-Baxter water droplet into a Wenzel type ice droplet during freezing was prevented. With the results of this study, the mechanism of ice adhesion to stainless steel was better understood in an effort to achieve practical icephobicity for engineering applications.

Keywords: Ion implantation; stainless steel; icephobicity; surface topography; surface chemistry.

* Corresponding author. Tel.: +64 21 026 298 54
E-mail address: thomas.loho@auckland.ac.nz

2351-9789
10.1016/j.promfg.2019.02.034

1. Introduction

By manipulating the wettability of solid surfaces, functional surface properties such as self-cleaning, anti-icing, anti-fogging, and anti-adhesive surfaces can be achieved [1,2]. These properties can be obtained by making the surface tend to hydrophobic with high advancing water contact angles (close to or greater than 90°) and low contact angle hysteresis [3,4]. When a water droplet sits on a surface, it could either penetrate into the asperities (Wenzel state) or sit on top of the asperities and/or air bubbles within the asperities (Cassie-Baxter state). Superhydrophobicity (a contact angle higher than 150°) is usually achieved by manipulating the surface chemistry and roughness of materials to force water droplets to be in the Cassie-Baxter state rather than the Wenzel state [1,3]. The general consensus is that high advancing contact angle and low contact angle hysteresis is obtained by creating surfaces with low surface energy and hierarchical micro-nano scale roughness [3]. Surfaces with high contact angles have big potential to be used for various applications such as paints, solar cells, windows, and textiles to prevent dirt contamination, ice accretion, and many other kinds of fouling [5,6].

Hydrophobic metals are of special interest due to their common use in many engineering applications. Although metals are generally hydrophilic with high surface energy and low water contact angle [7], it is possible to modify the surface of metals to create a durable superhydrophobic surface. Researchers have been able to create superhydrophobic surfaces on copper, aluminium, and alloys such as stainless steel by combining hierarchical micro-nano surface topography with low surface energy [8]. This has been achieved using various methods. Examples include chemical etching [8], coating with a lubricant impregnated surface [9], or ion implantation [10].

This study investigated the potential application of ion implantation technique to create an icephobic surface with low ice adhesion strength. The characterisation method for ice adhesion strength measurements were developed in the micro-nano scale and has been described elsewhere [11] in order to study the effect of nano-scale surface topography and chemistry modifications. Ion implantation on stainless steel using Xe^+ ions was used to modify surface topography and CF^+ ions to modify the surface chemistry. The ice adhesion strength measurement results are then discussed and compared to the surface topography and chemistry changes of the stainless steel.

Stainless steels (SS) are chosen as the substrate due to their widespread use in many practical engineering applications. This study focuses specifically on the two commonly used grade 304 and grade 316 stainless steels. The two grade stainless steels are almost identical in terms of physical and mechanical properties, but the grade 316 stainless steel contains approximately 2 − 3% Mo that protects it against corrosion in the presence of chloride and other industrial solvents. In this study, grade 316 stainless steel was used for surface topography modification studies and grade 304 stainless steel was used for surface chemistry modification studies. The main reason for this was to better understand the effect of surface chemistry changes in the relatively simpler chemical make-up of the grade 304 stainless steel as compared to grade 316.

2. Experimental

2.1. Ion implantation

The ion implanter consists of an ion source, a mass selector, an accelerating column, electrostatic lenses, and a target chamber. All of these components operate in high vacuum (approximately 10^{-4} to 10^{-6} Pa). The Penning gas ion source creates plasma of ionised atoms and electrons, from which positive ions are extracted using a magnetic field. The ion source is set to a high positive voltage so that ions leaving the source are accelerated towards the first grounded electrode of an Einzel lens, which also serves as an extraction cone. The electrostatic Einzel lenses then focus the beam to a few millimetres in diameter. The ion beam then passes through a 90° bending electromagnet where the specific type of ion to be implanted can be selected by adjusting the value of the magnetic field. At the GNS Science facilities where this study was undertaken, the electromagnet also provides further focusing of the beam to magnetic field gradients in this magnet. After the mass selector, the beam passed through a small aperture to limit the ion beam diameter to typically 10 to 12 mm. A magnetic quadrupole was used to adjust the focus of the ion beam on the target. A removable Faraday Cup was used to confirm the presence of the ion beam and measure the ion beam current at an intermediate position during the setting up of the ion implantation experiment. During implantation, the Faraday Cup was removed and the beam passes through two electrostatic steering plates to steer

the beam in the X and Y directions, enabling the beam to scan over the surface of the target sample. The Faraday cup is also used to rapidly cut the beam path to stop the implantation.

Low energy xenon ion implantation was done in order to clean surface impurities and create nano-scale roughness within the micro-scale grain structure of the metal [12]. Xenon was chosen as the inert gas ion source due to its high atomic mass (Ar = 131 g·mol^{-1}), hence leading to a higher sputtering yield than lighter noble gas. Thus, bombarding the stainless steel surface with xenon can significantly modify the surface topography of stainless steels [13].

Table 1. Ion implantation parameters used in this study. Maximum concentrations and expected sputtered depths were obtained from simulation results using the D-TRIM software [14].

Target	Sample name	Xe^+ ions fluence (ions·cm^{-2})	Incident ions angle (°)	Maximum Xe concentration (%)	Sputtered depth (nm·cm^{-2})
316 SS	XC	n/a	n/a	n/a	n/a
316 SS	X1	1×10^{16}	0	13.4	6.6
316 SS	X2	5×10^{16}	0	16.5	32.6
316 SS	X3	1×10^{17}	0	16.7	65.0
316 SS	X4	1×10^{17}	45	8.1	127.7
316 SS	X5	1×10^{18}	45	8.8	1280.9
Target	Sample name	CF^+ ions fluence (ions·cm^{-2})	Maximum C concentration (%)	Maximum F concentration (%)	Sputtered depth (nm·cm^{-2})
304 SS	FC	n/a	n/a	n/a	n/a
304 SS	F1	1×10^{15}	0.7	0.6	0.2
304 SS	F2	5×10^{15}	2.9	2.8	1.3
304 SS	F3	1×10^{16}	5.4	5.3	2.5
304 SS	F4	2×10^{16}	9.8	9.5	5.0
304 SS	F5	5×10^{16}	21.1	22.3	12.1
304 SS	F6	1×10^{17}	40.3	34.1	22.3
304 SS	F7	2×10^{17}	59.4	47.5	39.6
304 SS	F8	4×10^{17}	82.2	58.5	71.3
Target	Sample name	CF^+ ions fluence (ions·cm^{-2})	Maximum C concentration (%)	Maximum F concentration (%)	Sputtered depth (nm·cm^{-2})
X1	XF1	5×10^{16}	23.0	20.8	8.7
X2	XF2	5×10^{16}	23.3	20.4	9.6
X3	XF3	5×10^{16}	25.6	21.9	9.2
X4	XF4	5×10^{16}	22.5	20.5	10.3
X5	XF5	5×10^{16}	23.3	21.4	9.6

The samples for surface topography study were cut from a single 1 mm thick sheet of grade 316 stainless steel (316 SS) into six 10 × 12 mm rectangles. Xe^+ ions were extracted from a Penning ion source at an accelerating voltage of 20 kV for all samples and selected with the 90° mass analyser magnet. These ions were then implanted into the surface of five of these samples with different fluences (ions·cm^{-2}). Ion implantation was carried out at 0° and 45° angle of incidence to promote atomic sputtering. To limit a significant increase in the temperature of the samples, the ion beam current density for all ion implantation was kept within 7 to 10 μA·cm^{-2}. Simulations of the interaction between ions and atoms in the surface during the ion implantation process using were done with the Dynamic Transport of Ion in Matter (D-TRIM) software [14] with 20 keV energy ions. It was found that implantation ranges of approximately 7 nm and 5 nm for 0° and 45° incident ion angle respectively for Xe^+ ion implantation were expected. The control sample was labelled XC and the other samples were labelled X1 to X5.

For surface chemistry modification, CF^+ ions were implanted on the surface of the stainless steel substrates. These ions were selected in the 90° bending electromagnet and then implanted onto the substrates. Upon entering the surface, the C−F bond in the ion is very likely to break during the first collision in the cascade, breaking the ion

down into C (Ar = 12 g·mol^{-1}) and F (Ar = 19 g·mol^{-1}) atoms. The substrates for surface chemistry modification study were 12 mm diameter discs cut from a sheet of 1 mm thick grade 304 stainless steel (304 SS). These samples were labelled FC for the control sample and F1 to F5 for increasing ion fluence.

To further investigate the effect of surface topography and chemistry modifications, the second treatment of CF^+ ions implantation was also performed on the first batch of samples (X1 to X5) that had been bombarded with Xe^+ ions and had their surface topography modified with nano-scale pillars and ripple pattern. The same ion fluence of 5 × 10^{16} ions·cm^{-2} was implanted onto each of these samples, labelled XF1 to XF5 accordingly. Simulations for these samples were done for both C and F atoms, similar to the ones done with the CF+ ion implanted samples. However, in this case, the target layers for the simulations are stainless steel substrate with the addition of Xe atoms with the maximum concentration obtained from previous simulations for the Xe+ ion implanted samples.

All of the stainless steel substrates had a bright annealed (BA) surface finish that complies with the standard for a smooth, bright, reflective stainless steel surface according to the Standard Specification for General Requirements for Flat-Rolled Stainless and Heat-Resisting Steel Plate, Sheet, and Strip ASTM A480/A480M standard [15]. Table 1 shows the different ion beam treatment parameters used as well as the simulation results for the stainless steel substrates.

2.2. Sample characterisation

The nano-scale surface features of the samples were characterised by obtaining high-resolution images of 20 × 20 µm areas with 512 line scans using the FlexAFM (Nanosurf) Atomic Force Microscope (AFM). The surface topography images and line profiles were obtained using the software Gwyddion [16].

Surface chemistry characterisation was carried out using a Kratos Axis DLD X-ray Photoelectron Spectroscope (XPS) equipped with a hemispherical electron analyser. The photoelectron spectra were excited using a monochromatic Al Kα X-rays (1486.69 eV) running at 150 W. The analyser was set with pass energy of 80 eV and a dwell time of 0.044 s to acquire an average of 20 scans in 40 minutes. The instrument collected information from an area of 300 × 700 µm on the surface and was operating at a base pressure of 1.3 × 10^{-7} Pa. Survey scans revealed the elemental composition to a depth of 10 nm below the surface and core scans analyse the binding energy signals close to the known elements. Data analysis was carried out using the software CasaXPS (Casa Software Ltd.).

The micro-nano scale ice adhesion strength of the samples was measured using the novel nanoscratch technique described elsewhere [11]. Tests were done at −10°C surface temperature in air with an ambient humidity of approximately 35% and an ambient temperature of about 23°C. Humidity control was achieved using approximately 100 g of $CaCl_2$ desiccant placed near the testing rig inside the nanoscratch test chamber. Five measurements on different ice droplets on each sample were done in this study.

3. Results and discussions

3.1. Surface topography modification

20×20 µm area topography images with nano-scale resolution for selected samples obtained from AFM are shown in Figure 1a with sample line profiles shown in Figure 1b. RMS roughness (R_q) values were then measured from these line profiles. The XC sample showed a slightly rougher surface with R_q = 2.8 ± 0.1 nm than the FC sample with R_q = 1.8 ± 0.2 nm. Samples X1 to X4 showed similar R_q of approximately 5.1 ± 0.2 nm and sample X5 had a much higher R_q of 45.5 ± 4.3 nm. Samples F1 to F7 had similar R_q of around 2.3 ± 0.8 nm while sample F8 showed a slightly rougher surface with R_q of 4.1 ± 0.7 nm. Samples XF1 to XF4 had similar R_q of 3.3 ± 0.6 nm that are slightly smaller than the R_q values of samples X1 to X4. Sample XF5 showed an R_q value of 22.5 ± 3.6 nm that is smaller than the R_q value of sample X5.

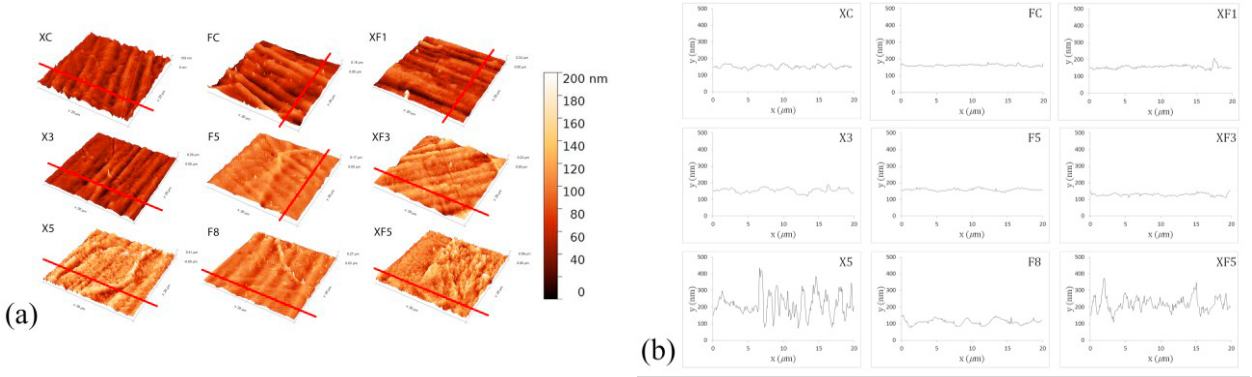

Figure 1. Selected (a) 3D 20 × 20 µm area surface topography and (b) 20 µm line profiles obtained from performing AFM on the ion implanted stainless steel samples. The line profiles were taken across polishing lines as indicated by the solid red line in each 3D profile.

3.2. Surface chemistry modification

The XPS survey scan spectra for some selected ion implanted samples are shown in Figure 2 and core level scan spectra in Figure 3. It can be seen from Figure 2a and Figure 3a that the Xe^+ ion implanted samples had very little Xe content as shown by the very small Xe peak (binding energy of around 669 eV [17]) on samples X1 to X5, where samples X4 and X5 with the 45° angle of incident ions show even smaller amounts of Xe atoms. This suggests that solid-state diffusion process occurred during the implantation, causing a much lower retained Xe concentration that was detected by the XPS spectra.

For the CF^+ ion implantation, there is no distinct peak detected on any of the ion implanted surfaces at the position of F−C bond (binding energy of around 688.0 eV [17]) and F−Fe bond (684.9 eV [17]) in the F 1s core level scan for the F5, F8, XF1, XF3, and XF5 samples. This result suggests that the F atoms were not covalently bonded with the surface atoms after they were dissociated from the CF^+ ions, making them prone to solid-state diffusion and leading to the very little amount observed.

On the other hand, the C 1s core scan result in Figure 3b show a slight increase in the intensity of the peaks at the position of C−F bond (289.0 eV) for samples F5, F8, XF1, XF3, and XF5 when compared to the control sample FC [17]. The spectra also show a slight increase in the intensity of peaks at the C−C bond (284.5 eV) and C−Fe bond binding energies (283.6 eV) [17], indicating the implantation of C atoms on the surface. Since it is unlikely that the C−F bonds in the CF^+ ions were retained during collision with the surface atoms, any C−F bond detected is more likely to be caused by the re-formation of those bonds by the implanted C and F atoms. However, the intensity of these peaks are too small for reliable quantification results from the spectra.

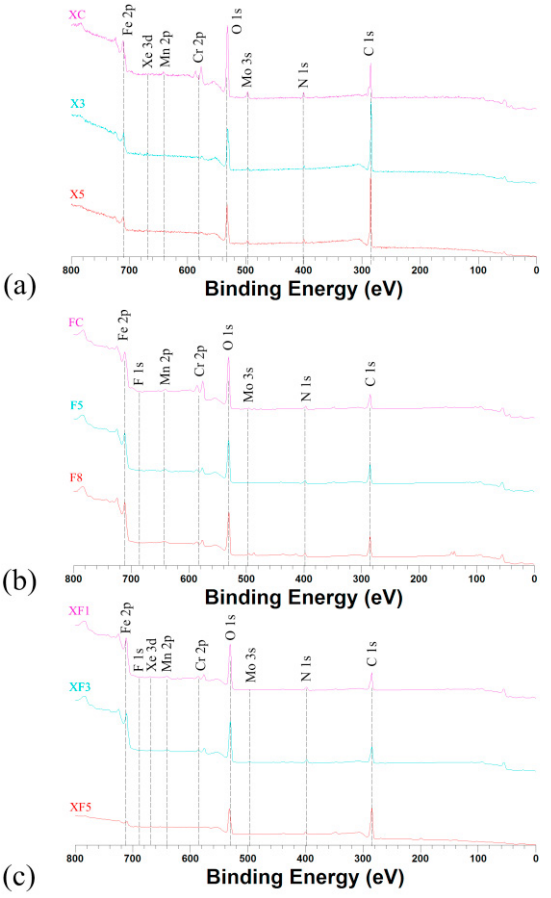

Figure 2. Selected XPS survey scan spectra on the (a) Xe+ ion implanted stainless steels, (b) CF+ ion implanted stainless steels, and (c) Xe+ and CF+ ion implanted stainless steels.

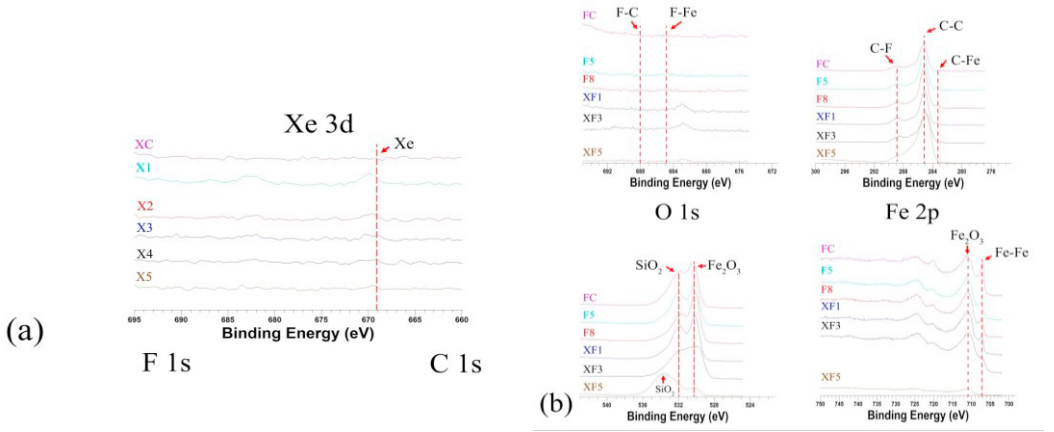

Figure 3. Selected XPS core scan spectra on selected elements on (a) Xe^+ ion implanted stainless steels and (b) selected CF^+ ion implanted stainless steels and Xe^+ and CF^+ ion implanted stainless steels.

The O 1s core level scan show peaks at the binding energies for Fe_2O_3 (530.2 eV) and SiO_2 (532.0 eV and 533.8 eV). The Fe 2p core level scan show peaks at the Fe−Fe (707.0 eV) and Fe_2O_3 (711.0 eV) binding energy positions [17]. The Fe−Fe peak shows the iron atoms in the steel crystal lattice and the Fe_2O_3 and SiO_2 peaks can be attributed to surface corrosion effects and silica contamination of the samples.

3.3. Ice adhesion strength changes

Figures 4a to 4c show the results of micro-nano scale shear ice adhesion strength measurement. The tests were done with a surface temperature of −10°C.

Surface topography and chemistry modifications were thought to likely be responsible for any changes in the micro-nano scale shear ice adhesion strengths measured. Figure 4a shows that for the Xe^+ ion implanted stainless steels, samples X1 to X4 had ice adhesion strengths around 3.7 ± 1.3 MPa, similar to the ice adhesion strength of the control sample XC of 5.7 ± 1.4 MPa. Sample X5 showed much higher ice adhesion strength of 24.3 ± 15 MPa, about three times higher than the ice adhesion strength of the control sample XC. However, this sample also showed much larger variation compared to the other Xe^+ ion implanted samples. The suggested mechanism behind this phenomenon is illustrated in Figure 5.

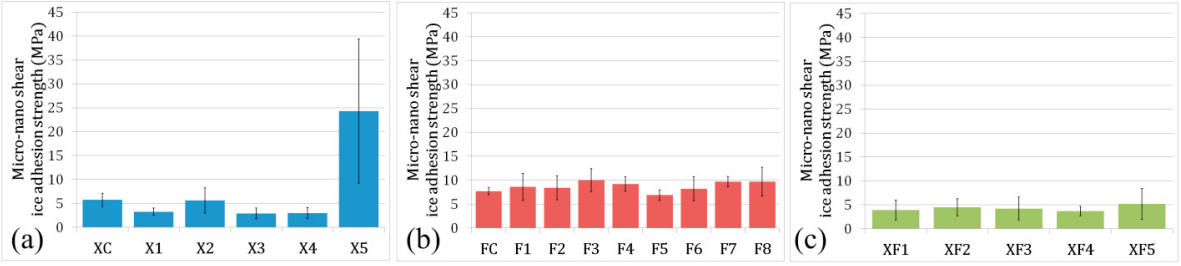

Figure 4. Micro-nano scale shear adhesive strength measurement results on (a) Xe^+ ion implanted samples, (b) CF^+ ion implanted samples, and (c) Xe^+ and CF^+ ion implanted samples. Error bars show the value for one standard deviation from five independent measurements.

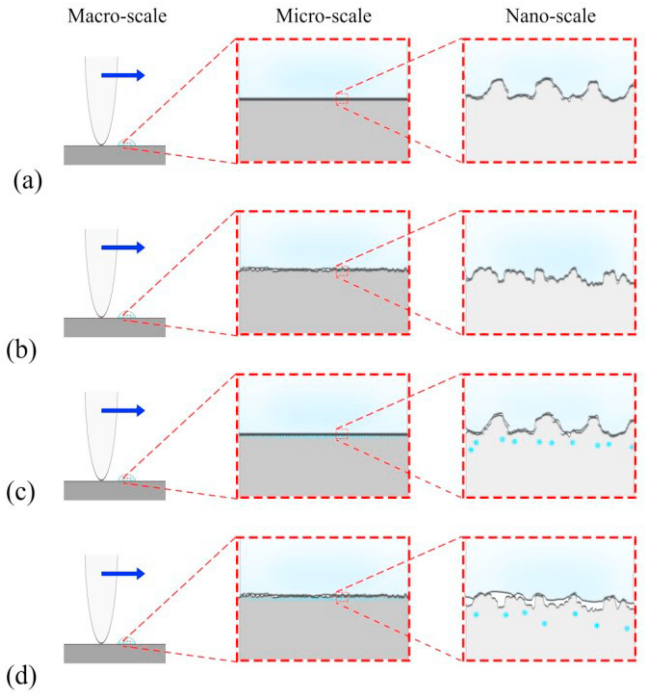

Figure 5. Illustrations suggesting the mechanism of ice adhesion during the micro-nano scale shear ice adhesion strength measurement testing on the (a) unmodified control sample and (b) surface topography modified samples, (c) surface chemistry modified samples, and (d) surface topography and surface chemistry modified samples.

Since XPS analysis revealed insignificant surface chemistry changes in the Xe^+ ion implanted samples, any change in ice adhesion strength of these samples was thought to be caused by surface topography effects. Comparing the roughness data with the micro-nano scale ice adhesion strength, a microscopic ice formed on a rougher surface has a much higher true contact area than a smooth surface for the same apparent contact area. Due to the small size of the ice droplet, it was suggested that it is more likely for the interface to have a Wenzel-type contact as illustrated in Figure 5b.

The insignificant effect of CF^+ ion implantation on the measured ice adhesion strengths of samples F1 to F8 compared to FC and samples XF1 to XF4 compared to samples X1 to X4 suggests that the implanted fluorine-rich hydrocarbons are not found in the peak of the asperities, as shown in Figures 5c and 5d. Moreover, XPS analysis revealed that there are only small amounts of the fluorine rich-hydrocarbons implanted onto the surface of these steels.

In Figure 5c, for a relatively flat and smooth surface that has been implanted with CF^+ ions (samples F1 to F8 and XF1 to XF4), the change in surface chemistry is insufficient to prevent the formation of a Wenzel-type contact at the ice-solid interface. It was thought that the slight expansion of water droplet during freezing overcame the lower surface energy caused by the surface chemistry change. This resulted in the expansion of water droplets into the space between asperities, pushing air bubbles out and creating a Wenzel- type water droplet. Because of this, the true area of contact in the ice-solid interface is relatively unchanged by the implantation of CF^+ ions onto the surface.

On the other hand, for a heavily nano-structured surface such as sample X5, the small amount of fluorine-rich hydrocarbons was thought to be sufficient to prevent the expansion of water droplets into the space between asperities during freezing, as shown in Figure 5d. This is thought to be because of much smaller spacing between asperities in nano-structured surfaces, resulting in a much smaller volume of water that had to be repelled by the surface in order to maintain a Cassie-Baxter type of contact at the ice-solid interface.

4. Conclusions

The process of low energy ion implantation with two different ion beams has been shown to modify the surface topography and surface chemistry of stainless steel. By creating three different types of surfaces using this ion implantation technique (surface topography modified, surface chemistry modified, and a combination of both) and characterising the ice adhesion strength of these samples, one can gain new insights into the mechanism of ice adhesion to metallic surfaces.

By studying the effects of surface topography and surface chemistry modifications through ion implantation on the ice adhesion strength of stainless steel, the mechanism of ice adhesion to metallic surfaces can be better understood. However, it is also acknowledged that this study has several limitations. Although it was thought that changes in the Xe^+ ion implanted samples are due to surface topography effects and changes in the CF^+ ion implanted samples are due to surface chemistry changes, there could also be some small changes in the surface chemistry of the Xe^+ ion implanted samples and changes in the surface topography of the CF^+ ion implanted

samples. It is also suggested in this study that the significant changes in the micro-nano scale ice adhesion strength from ion implantation was insufficient to make any significant changes in the macro-scale ice adhesion strength that is more representative of real-world situations. Nevertheless, this study has given new insights into the mechanism of how ice adheres to stainless steel surfaces.

Acknowledgements

This study was funded by the University of Auckland Doctoral Scholarship program and the Science Strategic Investment Fund from GNS Science, New Zealand.

References

[1] L. Makkonen, Ice Adhesion — Theory , Measurements and Countermeasures, J. Adhes. Sci. Technol. 26 (2012) 413–445. doi:10.1163/016942411X574583.

[2] T. Bharathidasan, S.V. Kumar, M.S. Bobji, R.P.S. Chakradhar, B.J. Basu, Effect of wettability and surface roughness on ice-adhesion strength of hydrophilic, hydrophobic and superhydrophobic surfaces, Appl. Surf. Sci. 314 (2014) 241–250. doi:10.1016/j.apsusc.2014.06.101.

[3] D. Quéré, Wetting and Roughness, Annu. Rev. Mater. Res. 38 (2008) 71–99. doi:10.1146/annurev.matsci.38.060407.132434.

[4] M. Nosonovsky, B. Bhushan, Roughness-induced superhydrophobicity: a way to design non-adhesive surfaces, J. Phys. Condens. Matter. 20 (2008) 225009–225039. doi:10.1088/0953-8984/20/22/225009.

[5] K. Golovin, S.P.R. Kobaku, D.H. Lee, E.T. DiLoreto, J.M. Mabry, A. Tuteja, Designing durable icephobic surfaces, Sci. Adv. 2 (2016). doi:10.1126/sciadv.1501496.

[6] W.S.Y. Wong, Z.H. Stachurski, D.R. Nisbet, A. Tricoli, Ultra-Durable and Transparent Self-Cleaning Surfaces by Large-Scale Self-Assembly of Hierarchical Interpenetrated Polymer Networks, ACS Appl. Mater. Interfaces. (2016) acsami.6b03414. doi:10.1021/acsami.6b03414.

[7] R. Menini, M. Farzaneh, Advanced Icephobic Coatings, J. Adhes. Sci. Technol. 25 (2011) 971–992. doi:10.1163/016942410X533372.

[8] L. Li, V. Breedveld, D.W. Hess, Creation of superhydrophobic stainless steel surfaces by acid treatments and hydrophobic film deposition., ACS Appl. Mater. Interfaces. 4 (2012) 4549–56. doi:10.1021/am301666c.

[9] P. Kim, T.-S.-S. Wong, J. Alvarenga, M.J. Kreder, W.E. Adorno-Martinez, J. Aizenberg, Liquid-infused nanostructured surfaces with extreme anti-ice and anti-frost performance, ACS Nano. 6 (2012) 6569–6577. doi:10.1021/nn302310q.

[10] S. Flege, R. Hatada, K. Baba, W. Ensinger, Fluorine and carbon ion implantation and deposition on metals by plasma source ion implantation, Surf. Coatings Technol. 206 (2011) 963–966. doi:10.1016/j.surfcoat.2011.03.100.

[11] T. Loho, M. Dickinson, Development of a novel nanoscratch technique for quantitative measurement of ice adhesion strength, IOP Conf. Ser. Mater. Sci. Eng. 348 (2018) 012003. doi:10.1088/1757-899X/348/1/012003.

[12] J. Kennedy, P.P. Murmu, E. Manikandan, S.Y. Lee, Investigation of structural and photoluminescence properties of gas and metal ions doped zinc oxide single crystals, J. Alloys Compd. 616 (2014) 614–617. doi:10.1016/j.jallcom.2014.07.179.

[13] J.S. Williams, J.M. Poate, Ion implantation and beam processing, Academic Press Australia, Sydney, 1984.

[14] I.R. Chakarov, S.S. Todorov, D.S. Karpuzov, Dynamic Monte-Carlo simulation of compositional change and atomic redistribution in multicomponent targets under ion bombardment, J. Phys. Chem. C. 69 (1992) 193–199.

[15] ASTM Standard A480/A480M, Standard Specification for General Requirements for Flat-Rolled Stainless and Heat- Resisting Steel Plate , Sheet , and Strip, ASTM Int. (1962). doi:10.1520/B0906-02R12.2.

[16] D. Necas, P. Klapetek, Gwyddion: an open-source software for {SPM} data analysis, Cent. Eur. J. Phys. 10 (2012) 181–188. doi:10.2478/s11534-011-0096-2.

[17] NIST X-ray Photoelectron Spectroscopy Database, NIST Standard Reference Database Number 20, Natl. Inst. Stand. Technol. Gaithersbg. MD, 20899. (2000). doi:10.18434/T4T88K.